Journal of Biomechanics Open 1 (2026) 100020

Contents lists available at ScienceDirect

Journal of Biomechanics Open

journal homepage: www.sciencedirect.com/journal/journal-of-biomechanics-open

From tissue to chondrocyte deformation: an *in silico* modeling for mechanistic understanding of zone-specific cartilage micro-mechanics

Saiful Islam [a], Malek Adouni [b], Asif Istiak [a], Tanvir R. Faisal [a,*]

[a] Dept. of Mechanical Engineering, University of Louisiana at Lafayette, USA
[b] Biomedical and Instrumentation Engineering, Abdullah Al Salem University, Khalidiya, Kuwait

ARTICLE INFO

Keywords:
Multiscale constitutive modeling
Fibril-reinforced poro-hyperelasticity
Finite element analysis
Strain-dependent permeability
Articular cartilage

ABSTRACT

Understanding how tissue-level loads are transmitted to the collagen network, non-fibrillar matrix, interstitial fluid, and cells of articular cartilage is key to identifying the mechanical signals that govern chondrocyte response. The extracellular matrix (ECM) is a hierarchical biphasic composite comprising type II collagen fibrils, proteoglycans, and interstitial fluid; with embedded chondrocytes and their pericellular matrix (PCM). The ECM exhibits depth-dependent architecture and mechanical behavior that is difficult to measure experimentally. Here, a multi-structural fibril-reinforced poro-hyperelastic (MS-FRPHE) finite element model was developed to connect tissue-level loading to cellular mechanics. Depth-dependent type II fibril orientation, fibril volume fraction, cell density, and cell morphology were embedded in a single finite-deformation framework. Calibrated by inverse finite element analysis, the model was independently validated against indentation and unconfined compression at 0.1% s^{-1} and 100% s^{-1} ($R^2 = 0.93$–0.98). Under 20% physiological compressive strain, the middle zone (MZ) exhibited peak ECM strain (≈0.74), exceeding the superficial (SZ) and deep (DZ) zones by 12% and 37%, respectively. Additionally, PCM strains consistently exceeded local ECM values, while chondrocyte size decreased by 56%, 49%, and 21% in the SZ, MZ, and DZ, respectively. The fibril network captured tension–compression nonlinearity, with peak stress of 3.5 MPa in surface-parallel SZ fibrils and negligible stress in vertical DZ fibrils, while pore pressure and fluid velocity showed steep depth-dependent gradients. Sensitivity and uncertainty analyses identified the chondrocyte and ECM moduli as most influential, with the zonal ordering of cell strain preserved throughout. This framework provides constituent-level predictions that are experimentally inaccessible, offering a quantitative foundation for studying cartilage micro-mechanics.

1. Introduction

How mechanical load is distributed within articular cartilage and ultimately delivered to its resident chondrocytes, determines whether the tissue is maintained or progressively degraded, making the cartilage mechanical environment a central concern for joint health (Shioji et al., 2014; Zhao et al., 2020). Articular cartilage is a hierarchically structured soft connective tissue, whose macroscopic (bulk) mechanical response emerges from coupled, finite-deformation interactions among a fibrillar collagen network, a charged proteoglycan-rich non-fibrillar matrix, interstitial fluid, and embedded chondrocytes. When subjected to mechanical loading, this constituent-level mechanical environment governs chondrocyte mechanotransduction, which is fundamental to cartilage homeostasis (Shioji et al., 2014; Zhao et al., 2020). Therefore, understanding how mechanical signals propagate from the cartilage tissue to individual cells provides key insights into the pathways by which chondrocytes detect and respond to their physical microenvironment.

The biphasic articular cartilage comprises 70–80% water and the solid phase, where chondrocytes and pericellular matrix (PCM), a specialized region surrounding each chondrocyte, embedded within the extracellular matrix (ECM) consisting of type II collagen fibrils and proteoglycans (Athanasiou et al., 2009; Mow, 1991; Responte et al., 2007). The microstructural architecture of articular cartilage varies by depth, dividing the tissue into three distinct zones: the superficial zone (SZ) with tangentially aligned fibrils and flattened chondrocytes at highest density, the middle zone (MZ) with randomly oriented fibrils and rounded cells, and the deep zone (DZ) with perpendicular fibrils and columnar chondrocytes at lowest density (Hunziker, 1992; Jadin et al., 2005; Youn et al., 2006). This heterogeneity substantially influences

* Corresponding author at: Department of Mechanical Engineering, University of Louisiana at Lafayette, LA 70503, USA.
E-mail addresses: md-saiful.islam1@louisiana.edu (S. Islam), asif.istiak1@louisiana.edu (A. Istiak), tanvir.faisal@louisiana.edu (T.R. Faisal).

https://doi.org/10.1016/j.jbmo.2026.100020
Accepted 5 August 2026
Available online 20 August 2026

mechanical behavior (Hunziker, 1992; Schinagl et al., 1997; Wang et al., 2001). The collagen network enables tension-compression nonlinearity and interstitial fluid pressurization critical for load support (Ateshian, 2009; Chahine et al., 2004), while the PCM modulates strain transmission to cells (Julkunen et al., 2009; Khoshgoftar et al., 2018). Although this structural hierarchy produces zone-specific mechanical environments at ECM, PCM, and cellular levels that govern mechanotransduction, experimental quantification of the individual mechanical contributions of fibrillar and non-fibrillar components *in vivo* remains difficult due to the coupled nature of cartilage mechanics across scales.

In silico modeling of cartilage by integrating finite element analysis (FEA) with multiscale frameworks has been widely used to simulate physiological behaviors like fluid flow and tissue deformation. Fibril-reinforced poroelastic (FRPE) models have successfully captured cartilage's dynamic and equilibrium behavior (Fortin et al., 2000; Julkunen et al., 2013; Li et al., 2009). Early FRPE models represented collagen through homogenized continuum formulation, transversely isotropic materials (Fortin et al., 2000; Julkunen et al., 2013; Li et al., 2009) or vector-based distributions (Pierce et al., 2009; Seifzadeh et al., 2011; Wilson et al., 2004; Wilson et al., 2005; Wilson et al., 2006). Subsequently, spring elements (Korhonen et al., 2003;Li et al., 1999 ; Shirazi & Shirazi-Adl, 2005) and membrane elements (Li et al., 1999; Shirazi & Shirazi-Adl, 2005) enabled explicit fibril deformation tracking, demonstrating that local collagen stresses depend critically on arcade-like fibril architecture. However, these fibril-focused models mostly ignored the non-fibrillar microstructural details, especially the cellular microenvironment. Therefore, we aim at developing a physics-based multiscale mechanical (FE) model by explicitly incorporating representative microstructural details to estimate how macro-strains translate into micro-strains on individual chondrocytes.

A few prior studies combined cellular level FE models with fibril reinforced constitutive formulations. Single-cell biphasic models (Federico et al., 2005; Kim et al., 2008) and multicell models (Halloran et al., 2018; Tanska et al., 2020) examined cellular responses within ECM constructs. Halloran et al. (Halloran et al., 2018) employed a biphasic neoHookean formulation without any collagen fibril network, with constant permeability and no osmotic swelling, and modeled eleven spherical chondrocytes embedded in MZ (transitional) only. Tanska et al. (Tanska et al., 2020) developed a multiscale framework combining FRPE tissue mechanics with anatomically distributed 21 chondrocytes confined to the SZ, implemented in a fully three-dimensional construct with quadrant symmetry. However, these studies were primarily limited to single zone and unable to capture the fibrillar stress, because the fibril network was represented in homogenized continuum form (a fibril-network modulus embedded in the constitutive law, without output of individual fibril stress (Tanska et al., 2020)). Furthermore, those models incorporating both cells and FRPE mechanics have assumed uniform cell shapes across zones (Halloran et al., 2018; Tanska et al., 2020), despite documented morphological variations in cells across the zones (Youn et al., 2006). Therefore, the primary goal of this study is to develop an FE framework by explicitly resolving discrete collagen fibril kinematics and capturing zonal variations in chondrocyte morphology, thereby providing a more mechanistic understanding of localized tissue micro-mechanics.

This study establishes an experimentally validated, multi-structural fibril-reinforced poro-hyperelastic (MS-FRPHE) finite element framework that simultaneously captures macro-scale tissue mechanics and micro-scale chondrocyte mechanics. By discarding homogenized continuum representations in favor of discrete geometric fibril elements and zone-specific cell morphologies alongside their distinct PCM, this model enables the decoupling of constituent-specific mechanical responses. Specifically, the framework yields highly localized, experimentally inaccessible predictions of i) strain gradients across the ECM, PCM, and cellular domains; ii) individual collagen fibril stress trajectories; iii) depth-dependent cell deformations, and iv) pore pressure and fluid velocity distributions across cartilage constituents. Ultimately, this high-resolution computational platform provides a robust quantitative foundation to investigate cartilage mechanobiology, pathological remodeling, and the mechanical regulation of chondrocyte function.

2. Materials and methods

2.1. Construction of finite element model

A 2D axisymmetric FE model of cylindrical cartilage explants used in experiments with dimensions of radius, $R \approx 1.5\ mm$ and height (cartilage thickness), $H \approx 1.2\ mm$ was constructed in Abaqus 6.14 (Dassault Systèmes). The FE construct comprises three spatially distinct zones: SZ, MZ, and DZ constituting 10%, 20%, and 70% of the cartilage thickness, respectively, along with zone-wise variations in chondrocyte, PCM, and major macromolecules of cartilage ECM—type II collagen fibrils, proteoglycans, glycosaminoglycans (GAGs) (Hunziker, 1992; Jadin et al., 2005). The zone-wise variations in the microstructural architecture of FE construct are shown in Table 1.

In this construct, the SZ was modeled with flattened chondrocytes oriented parallel to the surface, the MZ was modeled with round-shaped chondrocytes, and the DZ with columnar chondrocytes (Youn et al., 2006). The zonal variations in cell distribution were incorporated into the construct, with a cell density ratio of 3:2:1 in the SZ, MZ, and DZ, respectively (Fig. 1) (Hunziker et al., 2002; Ren et al., 2016). Furthermore, the orientation of type II collagen fibrils was preserved, with fibrils parallel to the surface in the SZ and perpendicular to the surface in the DZ. The fibrils in the MZ were modeled horizontally, vertically, and diagonally $\pm 45^{\circ}$ to simulate the random fibril distributions observed in this zone. The SZ, MZ, and DZ were modeled with fibril volume fractions of 15%, 18%, and 21%, respectively (Adouni et al., 2012; Faisal et al., 2019, 2023; Shirazi & Shirazi-Adl, 2008; Wilson et al., 2004). No fibrils were incorporated in chondrocytes, as collagen fibrils are absent within these cells (Nahian & Sapra, 2020); therefore, the fibrils were modeled around the cell without overlap (Table 1 and Fig. 1).

2.2. Fibril-reinforced poro-hyperelastic material model

A biphasic material constitutive model consisting of solid and fluid phases was implemented in this physics-based FE model. The solid phase comprised a porous hyperelastic non-fibrillar matrix (representing proteoglycans) reinforced with a non-linear elastic collagen fibril network (Julkunen et al., 2010; Suh & Spilker, 1994). The total stress tensor, $\boldsymbol{\sigma}_{tot}$ consists of the stress induced by both fibrillar network and non-fibrillar matrices in combination with fluid (pore) pressure (Julkunen et al., 2013; Pierce, 2022).

$$\boldsymbol{\sigma}_{tot} = \boldsymbol{\sigma}_{mat} + \sum_{i=1}^{tot} \boldsymbol{\sigma}_{f,i} - p\mathbf{I} \tag{1}$$

where $\boldsymbol{\sigma}_{mat}$is the stress tensor of the non-fibrillar matrix, $\boldsymbol{\sigma}_{f,i}$ is the stress tensor of a fibril i, p is the fluid pressure, and $\mathbf{I}$is the second order identity tensor. The FE implementation employed a hybrid modeling approach: (1) a user-defined material (UMAT) subroutine to describe the constitutive behavior of non-fibrillar matrix modeled with CAX4P continuum elements, and (2) Abaqus CONN2D2 connector elements with AXIAL connection to represent the type II collagen fibrils.

2.2.1. Finite strain kinematics

The deformation is characterized by the deformation graient tensor $\mathbf{F} = \partial\mathbf{x}/\partial\mathbf{X}$, mapping material points from the reference $(\mathbf{X})$to current $(\mathbf{x})$configuration. The Jacobian $J = \det(\mathbf{F}) > 0$ represents the local volume ratio. Following the multiplicative decomposition framework (Flory, 1961; Simo & Lubliner, 1986), the deformation gradient is decomposed into volumetric and isochoric parts:

$$\mathbf{F} = J^{1/3}\overline{\mathbf{F}} \tag{2}$$

Table 1
Spatial and morphological variations considered in constructing the FE model comprising chondrocyte, PCM, and ECM with type II collagen fibril heterogeneously oriented in different zones. Chondrocyte, PCM, and ECM were discretized using a 4-node axisymmetric porous element (CAX4P), whereas a 2-node connector element (CONN2D2) was used to represent collagen fibril.

Zone	Chondrocyte	PCM	ECM	Collagen fibril	Cartilage element (single quadrant)
SZ with no cell			40 μm, 20 μm		
SZ with cell		8 μm, 16 μm	12 μm, 24 μm		
MZ with no cell			40 μm, 20 μm		
MZ with cell		12 μm, 16 μm	16 μm, 24 μm		
DZ with no cell			40 μm, 40 μm		
DZ with cell		8 μm, 16 μm	12 μm, 24 μm		

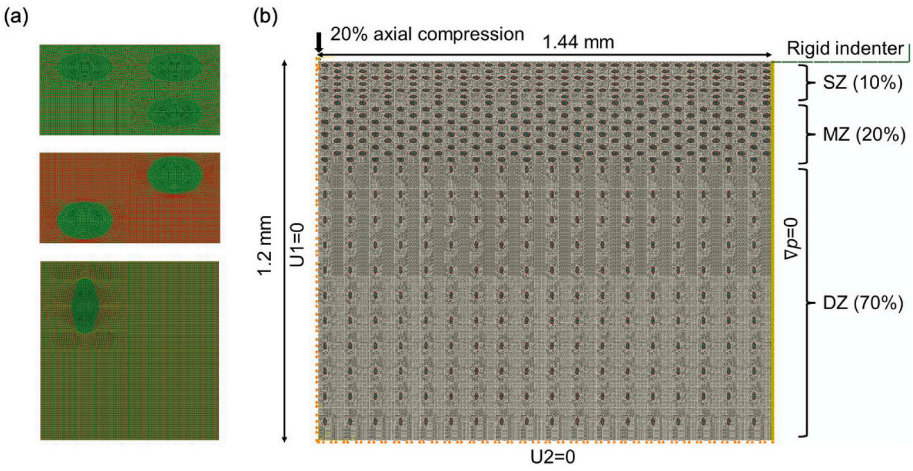

Fig. 1. (a) Zone-wise representative volume elements (RVE), the building block of the FE model following the 3:2:1 cell density across the SZ, MZ, and DZ, respectively. (b) 2D axisymmetric model of cartilage explant with three distinct zones and loading and boundary conditions.

where $\overline{\mathbf{F}} = J^{-1/3}\mathbf{F}$ is the isochoric (volume-preserving) deformation gradient with $\det(\overline{\mathbf{F}}) = 1$. The distortional left Cauchy-Green tensor is defined as:

$$\overline{\mathbf{B}} = \overline{\mathbf{F}}\overline{\mathbf{F}}^T = J^{-2/3}\mathbf{B} \tag{3}$$

where $\overline{\mathbf{B}} = \overline{\mathbf{F}}\overline{\mathbf{F}}^T$ is the left Cauchy-Green deformation tensor.

The deviatoric part of the deformation gradient is defined as,

$$dev(\overline{\mathbf{B}}) = \overline{\mathbf{B}} - \frac{1}{3}tr(\overline{\mathbf{B}})\mathbf{I} \tag{4}$$

$$\mathbf{C}_{nf.ijkl} = \frac{G}{J}\left[\frac{1}{2}\left(\delta_{ik}\overline{\mathbf{B}}_{jl} + \delta_{jk}\overline{\mathbf{B}}_{il} + \delta_{il}\overline{\mathbf{B}}_{jk} + \delta_{jl}\overline{\mathbf{B}}_{ik}\right) - \frac{2}{3}\left(\delta_{ij}\overline{\mathbf{B}}_{kl} + \delta_{kl}\overline{\mathbf{B}}_{ij}\right) + \frac{2}{9}tr(\overline{\mathbf{B}})\delta_{ij}\delta_{kl}\right] + \frac{K}{J}\delta_{ij}\delta_{kl} \tag{11}$$

The principal invariants are $\mathbf{I}_1 = tr(\mathbf{B}); \mathbf{I}_2 = \frac{1}{2}\left[(tr\mathbf{B})^2 - tr\left(\mathbf{B}^2\right)\right]; \mathbf{I}_3 = \det(\mathbf{B}) = J^2$.

2.2.2. Hyperelastic constitutive model

The non-fibrillar matrix behavior was governed by a compressible neoHookean strain energy function with decoupled volumetric-isochoric response.

$$\Psi = \Psi_{vol}(J) + \Psi_{iso}(\overline{\mathbf{B}}) = \frac{1}{2}K[\ln(J)]^2 + \frac{1}{2}G[tr(\overline{\mathbf{B}}) - 3] \tag{5}$$

where K and G denote the bulk and shear moduli, respectively, related to Young's modulus, E_{nf}, and Poisson's ratio, ν_{nf}. K and G are expressed as,

$$G = \frac{E_{nf}}{2(1+\nu_{nf})} \tag{6a}$$

$$K = \frac{E_{nf}}{3(1-2\nu_{nf})} \tag{6b}$$

2.2.3. Cauchy stress tensor

The effective Cauchy stress tensor $\boldsymbol{\sigma}$ was obtained from the strain energy function (Eq. 5) via the standard relation $\boldsymbol{\sigma} = J^{-1}\mathbf{B}.\partial\Psi/\partial\mathbf{B}$. For the neoHookean model,

$$\boldsymbol{\sigma}_{nf.ij} = J^{-1}\left[G\left(\overline{\mathbf{B}}_{ij} - \frac{1}{3}\overline{\mathbf{B}}_{kk}\delta_{ij}\right) + K\ln(J)\delta_{ij}\right] \tag{7}$$

2.2.4. Glycosaminoglycan swelling pressure

The osmotic swelling contribution from the negatively charged GAGs was modeled using a phenomenological volume-dependent formulation (Oungoulian et al., 2007; Sajjadinia et al., 2019):

$$\boldsymbol{\sigma}_{GAG} = \alpha_1\left(\frac{1}{J}\right)^{\alpha_2}\mathbf{I} \tag{8}$$

where $\alpha_1 = 0.060\,MPa$ and $\alpha_2 = 3.22$ are material constants (Sajjadinia et al., 2019). This formulation captures the concentration-dependent nature of proteoglycan-induced swelling pressure, as tissue compression $(J < 1)$ increases the fixed charge density, thereby elevating the osmotic pressure. Compared to the ideal Donnan equilibrium model, this phenomenological approach directly relates swelling pressure to local volume change without requiring explicit ion concentration calculations, while maintaining thermodynamic consistency.

The total effective stress of the non-fibrillar matrix computed by the UMAT comprises both contributions,

$$\boldsymbol{\sigma}_{mat} = \boldsymbol{\sigma}_{nf} + \boldsymbol{\sigma}_{GAG} \tag{9}$$

2.2.5. Consistent tangent modulus

The spatial elasticity tensor (material Jacobian) required for implicit Newton-Raphson iteration was derived analytically. The complete fourth-order tangent modulus comprises neoHookean and GAG contributions.

$$\mathbf{C}_{mat} = \mathbf{C}_{nf} + \mathbf{C}_{GAG} \tag{10}$$

where the neoHookean contribution is,

and the GAG contribution to the tangent modulus, derived from the linearization of the swelling pressure, is,

$$\mathbf{C}_{GAG.ijkl} = \alpha_1(\alpha_2 - 1)J^{-\alpha_2}\delta_{ij}\delta_{kl} + \alpha_1 J^{-\alpha_2}\left(\delta_{ik}\delta_{jl} + \delta_{il}\delta_{jk}\right) \tag{12}$$

2.2.6. Fluid phase

Darcy's law (Holmes & Mow, 1990) was employed to describe intra-tissue fluid flow within the porous matrix as follows:

$$q = -k\nabla p \tag{13}$$

where q is the rate of fluid flow, k is the (hydraulic) permeability of the materials, and ∇p is the (fluid) pressure gradient. Deformation within the porous material leads to alterations in the void ratio, which represents the ratio of fluid volume to solid volume, thereby causing changes in permeability (Van der Voet, 1997). The strain-dependent permeability, k is expressed as.

$$k = k_o\left(\frac{1+e}{1+e_o}\right)^M \tag{14}$$

where k and k_o represent the current and initial permeability, e and e_o represent the current and initial void ratio, respectively, M is a positive constant describing the void-ratio dependency of permeability (Grillo et al., 2017; Van der Voet, 1997; Wilson et al., 2004).

2.2.7. Collagen fibrils

In the proposed FE construct, the fibrillar network was modeled with Abaqus connector elements (CONN2D2) with AXIAL connection type. The AXIAL connection provides a translational degree of freedom along the line connecting two nodes specially designed for fiber-like structures. The connector's local direction was computed as,

$$\mathbf{e}_1 = \frac{\mathbf{x}_b - \mathbf{x}_a}{\|\mathbf{x}_b - \mathbf{x}_a\|} \tag{15}$$

The connector properties representing each fibril were defined by force-displacement relationships derived from the nonlinear stress-strain mechanical property of individual collagen fibers, as reported in prior studies (Haut & Little, 1972; Morgan, 1960; Shirazi & Shirazi-Adl, 2005). For an individual fibril, the force was calculated employing zone-wise fibril volume fractions, the number of fibrils, and the surface area as follows,

$$F_{fibril} = \frac{(\nu_f \times \sigma_f \times A_z)}{N_f} \tag{16}$$

where ν_f is the zone-wise fibril volume fraction (mentioned in Section 2.1), σ_f is the fibril stress corresponding to the strain obtained

from (Haut & Little, 1972; Morgan, 1960; Shirazi & Shirazi-Adl, 2005), and A_z is the zone-wise surface area, and N_f represents the number of fibrils in each zone. Accordingly, the values were $A_z = 0.1728\ mm^2$ and $N_f = 2862$ in SZ, $A_z = 0.288\ mm^2$ and $N_f = 31356$ in MZ, and $A_z = 1.2672\ mm^2$ and $N_f = 15660$ in DZ. The relative displacement (change in fibril length) of the individual fibril was calculated as follows,

$$\Delta L_f = \varepsilon_f \times L_o \tag{17}$$

where ΔL_f is a change in fibril length, L_o is the original length of an individual fibril, and ε_f is the strain values obtained from the literature (Haut & Little, 1972; Morgan, 1960; Shirazi & Shirazi-Adl, 2005) as well.

Collagen fibrils resist tensile loads only (Eq. 18). This tension only behavior was enforced through the non-linear connector behavior defined by force vs displacement tabular data in Abaqus.

$$F_f = f(\Delta L) for \Delta L > 0; F_f = 0 for \Delta L \leq 0 \tag{18}$$

The total internal force at each node combines the contributions from both continuum elements and connector elements through structural level assembly,

$$\mathbf{f}_{\text{int}} = \int_{\Omega} \mathbf{B}^T \boldsymbol{\sigma}_{nf} dV + \sum_i F_{f,i} \mathbf{n}_{f,i} \tag{19}$$

where $\mathbf{B}$ is the strain-displacement matrix, $\boldsymbol{\sigma}_{nf}$ is the UMAT Cauchy stress, $F_{f,i}$ is the axial force in connector i, and $\mathbf{n}_{f,i}$ is the fibril direction vector. The first integral represents continuum element contributions, and the summation represents discrete connector forces at shared nodes. Global equilibrium is achieved by.

$$\mathbf{F}_{ext} - \mathbf{F}_{\text{int}}(\mathbf{u}) = \mathbf{0} \tag{20}$$

where $\mathbf{F}_{ext}$ is the external force vector, and $\mathbf{F}_{int}(\mathbf{u})$ is the internal force vector as a function of displacement. ABAQUS solves this nonlinear system using the Newton-Raphson method, with the tangent stiffness matrix assembled from both UMAT contributions (via DDSDDE) and connector element stiffnesses (derived from the slope of tabular force-displacement data).

2.2.8. Material properties

Based on the hyperelastic material model (Eq. 2 to Eq. 12), Young's modulus, E_{nf}, and Poisson's ratio, ν_{nf}, a UMAT subroutine was developed for each element set including ECM, PCM, and cell of the non-fibrillar matrix. A permeability look up table was created using Eq. 14 with corresponding $M, k_o, e,$ and e_o values for ECM, PCM, and cell (Table 2), and the values were incorporated in the material model eventually. The initial void ratio e_o was fixed to 4.0, and the value of M was considered 7.1 (Wilson et al., 2004). An inverse FEA (FEA) (optimization) (Fig. 2.) was implemented to calibrate the parameters (E_{nf}, ν_{nf}, k_o) of the non-fibrillar matrix. Initial ranges of these parameters were obtained from prior studies (Table 2). The Levenberg-Marquardt algorithm was used to optimize the material parameters. Of these, only the modulus and Poisson's ratio of the ECM, PCM, and cellular non-fibrillar matrices together with the initial permeability of the ECM were calibrated within the lower and upper bound as prescribed in Table 2; the pericellular and cellular permeabilities were tied to the extracellular value by fixed ratios. The collagen fibril properties and GAG swelling constants were not calibrated, rather they were prescribed from independent studies. The objective function of the optimization routine minimized the normalized mean squared error between the simulated and experimental data, which was modified with a weighting factor resulting from peak data points as follows,

$$\delta\overline{F} = \frac{1}{n}\sum_{i=1}^{n}\left(\frac{F_i^{sim} - F_i^{\exp}}{F_i^{\exp}}\right)^2 + w\frac{1}{m}\sum_{j=1}^{n}\left(\frac{F_{j,p}^{sim} - F_{j,p}^{\exp}}{F_{j,p}^{\exp}}\right)^2 \tag{21}$$

where F_i^{sim} and $F_i^{\exp}$ are simulated and experimental force values, $F_{j,p}^{sim}$ and $F_{j,p}^{\exp}$ are peak force values obtained from the simulation and experiment, respectively; and n and m correspond to the total number of data points and number of peak data points ($m = 1$), respectively. Afterwards, the simulations were conducted with calibrated material properties to validate against experiments with two different loading configurations under slow and fast strain rates. (See Fig. 3.)

2.3. FE model with boundary and loading conditions

The 2D tissue model was meshed with 4-node axisymmetric porous element (CAX4P). The mesh size of the FE model underwent sensitivity analysis until a 5% difference in the reaction force was achieved. Unconfined compression was simulated using a flat indenter with 4.5 mm diameter, whereas the indentation was simulated with a 1 mm flat indenter diameter. Both indenters were modeled as a rigid body in contact with the cartilage's top surface. Displacement boundary conditions (BCs) were applied following the experimental set-up. The bottom nodes were constrained in y-direction, and the axisymmetric axis nodes were fixed along x-direction (Fig. 1). Zero pore pressure was prescribed at the outer surface of the cartilage, allowing fluid outflow through this boundary (surface).

All the simulations were conducted in a desktop workstation with intel core-i7 processor, 64 GB of Ram, and 30 GB of NVIDIA GeForce RTX 3080 GPU. The parametric calibration by inverse FEA required several iterations and took about 10 to 15 days depending on initial value. A single simulation of the calibrated model took about 24 to 30 h.

2.4. Sensitivity and uncertainty analyses

A one-at-a-time sensitivity analysis was performed on eight model parameters $(E_{ECM}, E_{PCM}, E_{cell}, k_o, zone-wise\ \nu_f\ in\ SZ, MZ, DZ, and\ \nu_f{\cdot}\sigma_f)$ comprising 24 additional FE simulations. The quantity of interest was the zone-averaged chondrocyte compressive strain at peak load, the metric on which the constituent-level conclusions rest. Each parameter (Y) was perturbed by ±20% about its calibrated value with all others held fixed, and a normalized sensitivity index, $S = [Y(+20\%) - Y(-20\%)]/(0.4 \times Y_{base})$ (Hamby, 1995), was evaluated for each zone. The index is dimensionless and therefore directly comparable across parameters of different units; a ±20% perturbation represents realistic uncertainty as it keeps each parameter within the upper and lower bounds reported in Table 2.

By employing a first order second moment (FOSM) framework together with the FE models, the study uses a first-order Taylor series approximation to estimate how those input variations propagate through the system. For independent inputs, this combination is evaluated using the following variance equation:

$$CV(Y)^2 = \sum S^2 \times CV(X)^2 \tag{22}$$

where $CV(X)$ is the coefficient of variation of each input, S is the sensitivity index, and $CV(Y)$ is the coefficient of variation of output. By combining these inputs, the model produces a predicted zone-averaged chondrocyte compressive strain. This gives an explicit statistical confidence interval around the strain experienced by the cells in different zones (e.g., SZ, MZ, and DZ of cartilage) despite baseline uncertainties in the tissue's mechanical properties.

Table 2
Typical range of material parameters for ECM, PCM, and cell (Darling et al., 2010; Tanska et al., 2020).

Parameter	ECM	PCM	Cell
$E_{nf}\ (MPa)$	(0.1–3.0)	(0.014–0.31)	(0.001–0.023)
ν_{nf}	(0.04–0.45)	(0.04–0.48)	(0.01–0.48)
$k_o\ (10^{-15} m^4 N^{-1} s^{-1})$	(0.6–6.0)	$0.1 \times k_{o,ECM}$	$100 \times k_{o,ECM}$

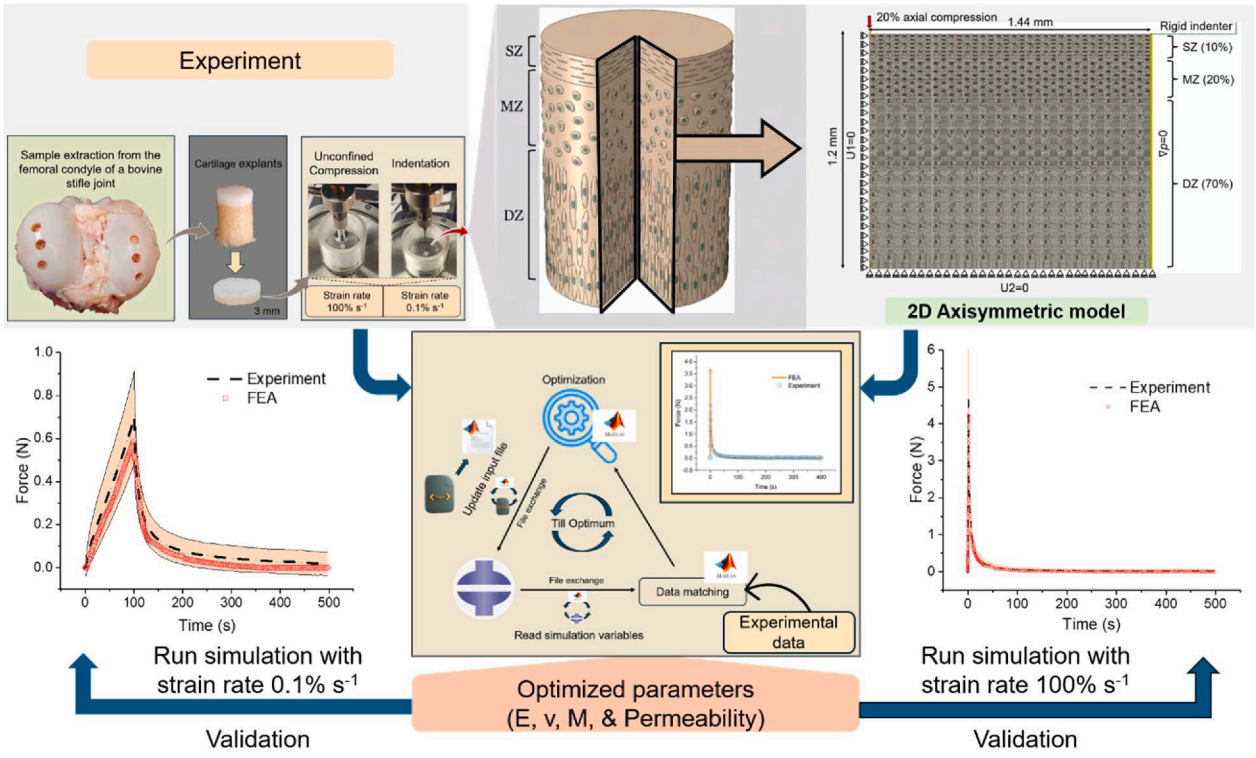

Fig. 2. Schematic of the integrated experimental-computational framework adopted in this study. The framework comprises four stages: (Top left) Experimental characterization; (Top right) Construction of a detailed FE model incorporating depth-dependent zonal heterogeneity; (Center) Calibration of material parameters via FEA; and (Bottom left and right) Model validation against independent experimental stress-relaxation data for slow (0.1% s^{-1}) and fast (100% s^{-1}) strain rate.

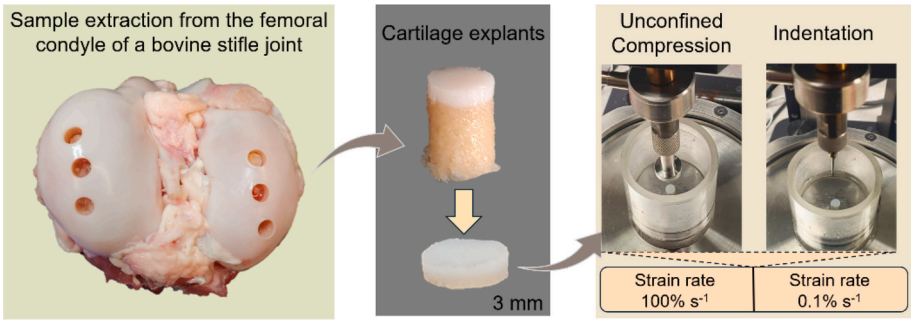

Fig. 3. Experimental workflow for cartilage mechanical characterization: sample extraction from bovine femoral condyle, preparation of cylindrical explants (3 mm diameter), and mechanical testing under unconfined compression (100% s^{-1} strain rate) and indentation (0.1% s^{-1} strain rate) configurations.

2.5. Experiments

The experimental protocol was followed as per our group's prior study (Istiak et al., 2025a) and briefly described herein.

2.5.1. Sample preparation

Fresh knee joints were collected from six bovines aged 18–30 months from a local slaughterhouse. Cylindrical osteochondral disks were harvested from 12 bovine femoral condyles using 3 mm diameter single use osteochondral autograft transfer system (Arthrex. Inc. USA). Samples from different subjects were mixed to avoid bias. Cartilage thickness was measured from high resolution image of the disk using ImageJ (National Institute of Health). 12 Cartilage disks with thickness of 1.2 ± 0.2 mm showing no visible defect on the surface were selected for mechanical testing. Cartilage was cut adjacent from the subchondral bone carefully with sharp surgical blade and the disks were wrapped in the phosphate-buffered saline (PBS) soaked gauge and stored in − 20^{o}C. The samples were thawed once (Szarko et al., 2010) in − 4$^{o}C$and kept in room temperature for 45 min in the PBS filled vials prior to mechanical testing.

2.5.2. Mechanical testing

All the mechanical tests were conducted by a Mach-1 v500c micro-mechanical tester, (Biomomentum Inc.). The lower surface of each cartilage disk was attached to the sample holder using liquid instant superglue. Samples were submerged in PBS to keep them hydrated during the mechanical tests. One-step stress relaxation test was conducted via two different loading configurations—unconfined compression and indentation under slow (0.1%/s) and fast (100%/s) strain rate. A non-porous flat platen with 4.5 mm diameter and a 1 mm diameter flat indenter were used for unconfined compression and indentation tests, respectively. 5 kPa pre-stress was applied before compression to ensure good contact between the platen and cartilage surface. Cartilages were compressed either 20% (calibration) or 10% (validation), that fall within the typical physiological loading range (Park et al., 2004), before attaining the 400 s of relaxation stage. Between every consecutive test,

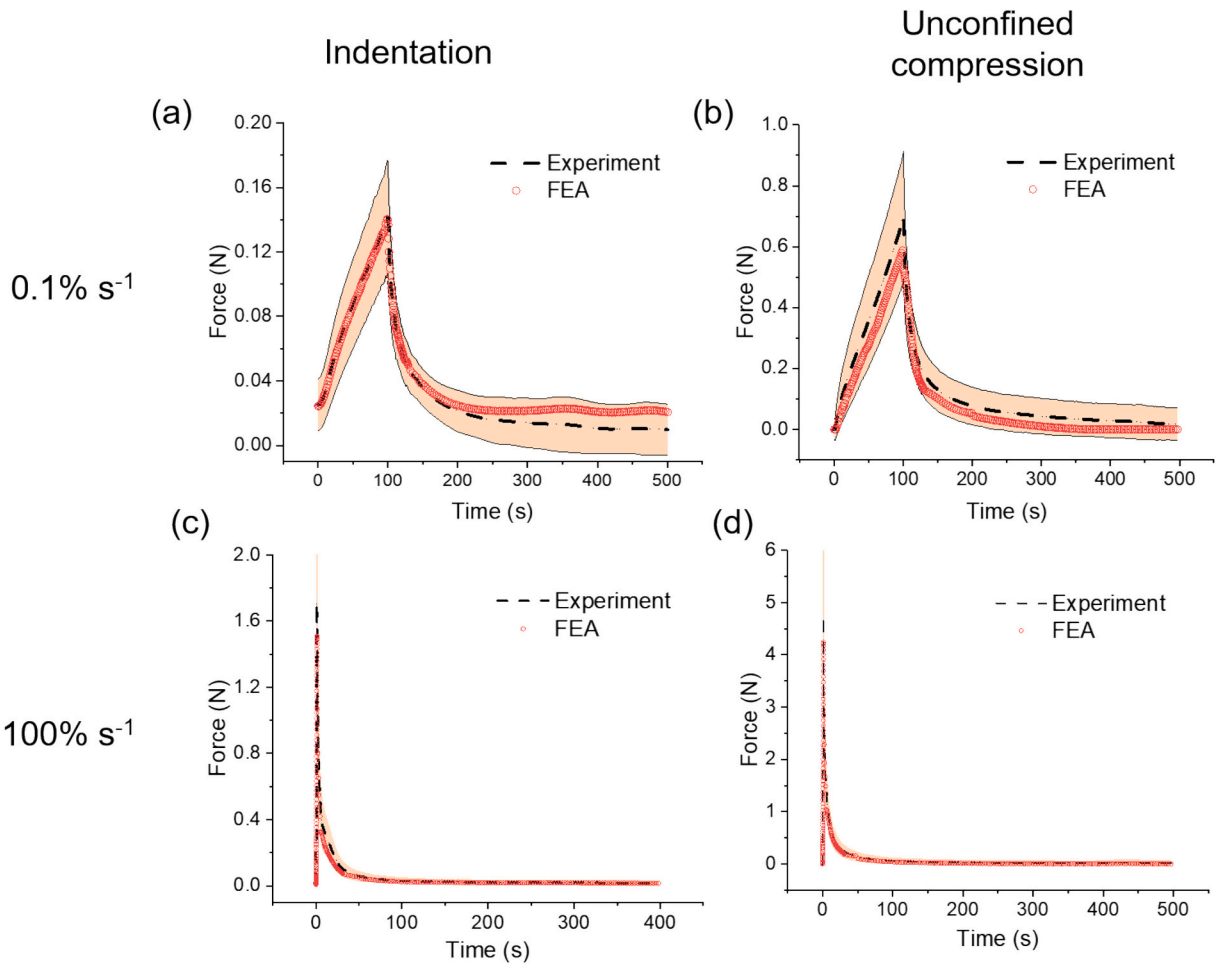

Fig. 4. Comparison of experimental and FEA predicted force-time responses during stress-relaxation testing under different testing configurations. Shaded bands represent experimental variability ($n = 12$). (a) Indentation and (b) unconfined compression at 0.1% s^{-1} strain rate, (c) indentation and (d) unconfined compression at 100% s^{-1} strain rate.

each sample was preserved in a serum-free medium at an incubated environment with37^oC and 5% CO_2 for shape recovery and avoid degradation (Istiak et al., 2025b).

3. Results

3.1. Experimental validation

The MS-FRPHE model was validated by comparing simulated force-time response against experimental measurements across four testing configurations comprising slow (0.1% s^{-1}) and fast (100% s^{-1}) strain rates and two loading configurations (indentation and unconfined compression) (Fig. 4). Calibrated material parameters from unconfined compression with 20% compressive strain at 100% s^{-1} strain rate were used in all the independent simulations for validation.

At slow strain rate (0.1% s^{-1}), the experimental (mean) peak force of 0.14 ± 0.03 N was accurately predicted by the MS-FRPHE model (0.13 N) during indentation test (Fig. 4a) with a coefficient of determination (R^2) of 0.98. For unconfined compression, the experimental peak force reached 0.70 ± 0.21 N compared to the predicted value of 0.59 N, with $R^2 = 0.93$ (Fig. 4b).

At fast strain rate (100% s^{-1}), both loading configurations exhibited substantially higher peak forces due to rapid fluid pressurization. Indentation produced an experimental peak force of 1.70 ± 0.42 N versus a predicted value of 1.51 N, with $R^2 = 0.97$ (Fig. 4c), and unconfined compression generated the highest peak force of 4.74 ± 1.58 N experimentally, with the model predicting 4.24 N and $R^2 = 0.98$ (Fig. 4d). Although the FE model was validated against 4 different testing configurations, the results in the following sections are shown for unconfined compression with 20% compressive strain at 100% s^{-1} strain rate.

3.2. Strain gradient in non-fibrillar constituents (ECM, PCM, and chondrocytes)

Analysis of zone-specific strain distributions during unconfined compression revealed distinct mechanical responses across the cartilage depth in the ECM, PCM, and chondrocytes. The compressive logarithmic strain distribution illustrated zone-specific strain variations in non-fibrillar cartilage components (Fig. 5a). The peak ECM strain of approximately 0.74 was observed at MZ, exceeded the SZ strain (≈ 0.66) by 12% and the DZ strain (≈ 0.54) by 37%. The PCM exhibited elevated strain levels compared to ECM across all the zones. In SZ, PCM strain reached approximately 1.08, representing a 63% increase over the local ECM value (≈ 0.66). MZ showed a similar pattern, with PCM strain (≈ 1.05) exceeding ECM strain (≈ 0.74) by approximately 42%. However, in DZ, PCM strain (≈ 0.65) demonstrated a 20% increase over ECM strain (≈ 0.54), reflecting a more uniform mechanical environment compared to the SZ and MZ. Chondrocytes in SZ experienced the highest strain (≈ 1.21), surpassing the local PCM strain (≈ 1.08) by 12% and the ECM strain (≈ 0.66) by 83%. MZ chondrocytes strain (≈ 1.14) exceeded PCM strain (≈ 1.05) by approximately 9%, whereas the maximum strain

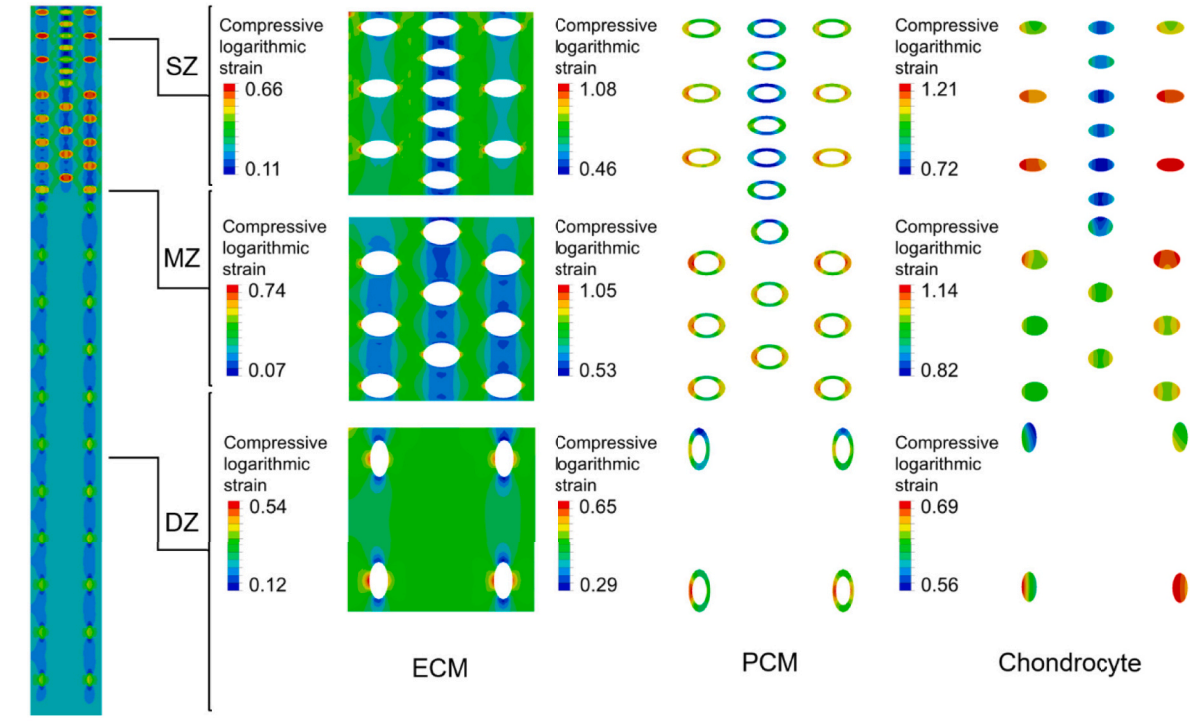

(a) Zone-wise contour plot of compressive logarithmic strain in ECM, PCM, and chondrocyte

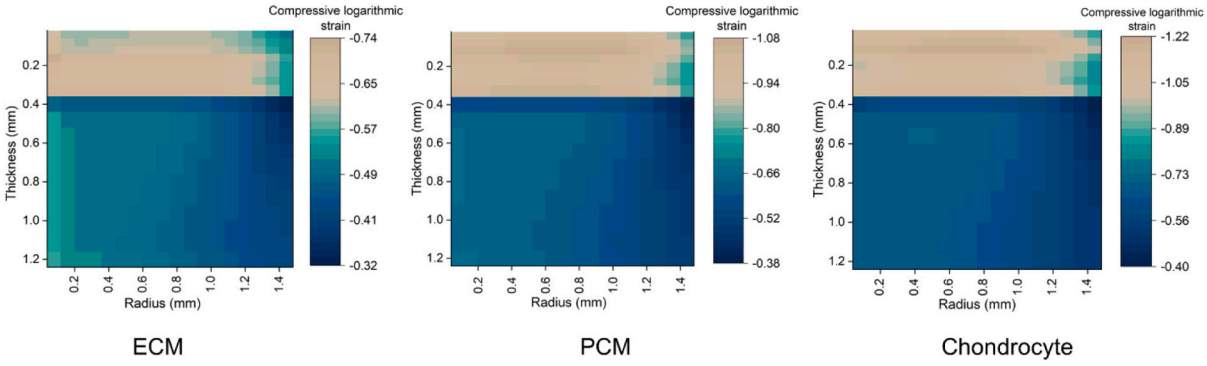

(b) Mapping of strain gradient against cartilage thickness and radius in ECM, PCM, and chondrocyte

Fig. 5. Zone-wise contour plot of compressive logarithmic strain (a) and mapping of strain against cartilage thickness and radius (b) in ECM, PCM, and chondrocyte. Thickness of SZ: 0–0.12 mm, MZ: 0.12–0.36 mm, and DZ: 0.36–1.2 mm. (a) Zone-wise contour plot of compressive logarithmic strain in ECM, PCM, and chondrocyte. (b) Mapping of strain gradient against cartilage thickness and radius in ECM, PCM, and chondrocyte.

(≈ 0.69) in DZ chondrocytes was comparable to the surrounding PCM strain (≈ 0.65).

Strain mapping revealed highly heterogeneous, radially varying and depth-dependent mechanical behavior across the three non-fibrillar constituents (Fig. 5b). Peak ECM strain was observed near the center axis, where the load was applied, and decreased toward the periphery. However, PCM and chondrocytes in the mid-radial location were subjected to the highest compressive logarithmic strain.

3.3. Fibrillar response

Stress contour in the fibrillar network in the MS-FRPHE model (Fig. 6) demonstrated compression-tension nonlinearity with a maximum stress of ~3.5 MPa in type II collagen fibrils in SZ, 1.2 MPa in MZ with 65.7% reduction from SZ, and negligible stress in DZ fibrils. The lower stress in the type II collagen fibrils of the MZ compared to the SZ reveals that the transition zone (MZ) effectively resists and redistributes compressive loads.

3.4. Zone-specific cellular deformation

The chondrocytes exhibited zone-specific distinct cellular deformation patterns (Fig. 7). SZ chondrocytes experienced the maximum size reduction (56%), followed by MZ cells (49%), while DZ chondrocytes underwent modest changes (21%) (Fig. 7a). The aspect ratio changes are particularly striking, with substantial increases in both SZ 3.6 (initial 2.0) and MZ 2.4 (initial 1.33), contrasting with a decrease in DZ 1.07 (initial 2.0) (Fig. 7b).

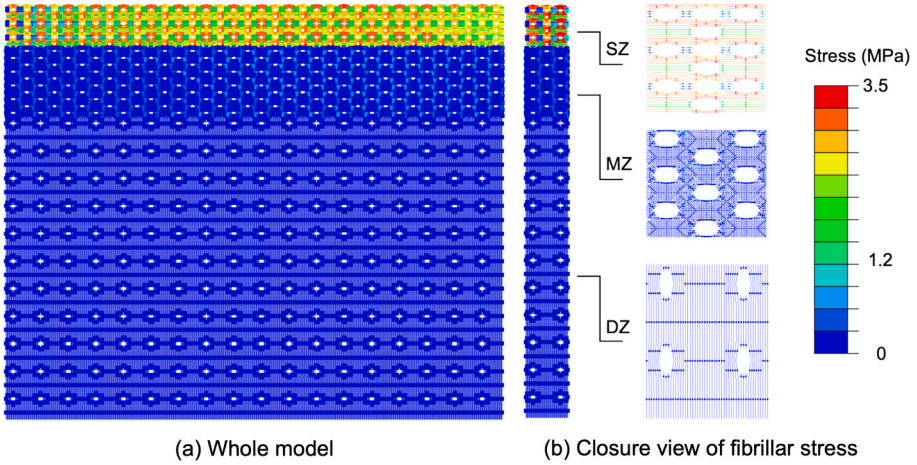

Fig. 6. (a) Stress distributions in type II collagen fibril network in (a) cartilage tissue and (b) the three zones (SZ, MZ, DZ) for a closure view.

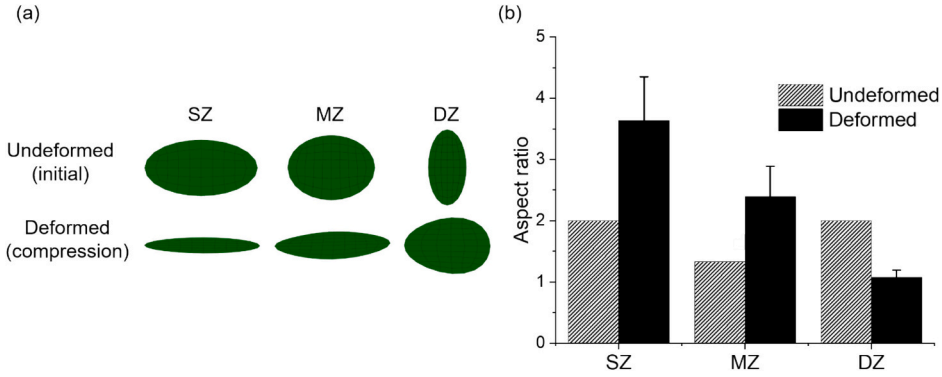

Fig. 7. Zone-wise comparison of shapes (a) and mean aspect ratio (deformed to undeformed shape) (b) of chondrocytes before and after compression. The error bar in bar plot indicates the standard deviation of the aspect ratio variability.

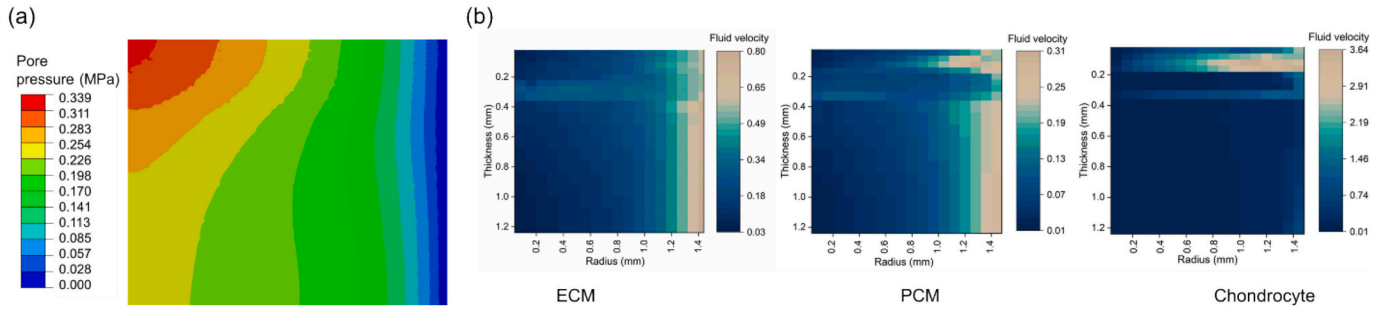

Fig. 8. (a) Pore pressure distribution in articular cartilage subjected to 20% of strain under unconfined compression. (b) Fluid velocity distributions across cartilage components. Thickness of SZ: 0–0.12 mm, MZ: 0.12–0.32 mm, and DZ: 0.32–1.2 mm.

3.5. Poromechanical fluid response

The poromechanical behavior of articular cartilage under unconfined compression was depicted through the spatial distributions of both pore pressure (Fig. 8a) and fluid velocity (Fig. 8b) within ECM, PCM, and chondrocytes.

3.5.1. Pore pressure distribution

The spatial distribution of pore pressure across cartilage displayed distinct zonal and radial variations (Fig. 8a), demonstrating the tissue's biphasic response to compressive loading. SZ showed highest pore pressure of ~0.34 MPa at its center, declining axially to 0.15–0.25 MPa in MZ and below 0.10 MPa in DZ. Radially, pressures decreased from the axis toward the periphery in both SZ (~0.34 to ~0.25 MPa) and MZ (highest near the center, lower at the edge), whereas the DZ remained uniformly low. Overall, the steep axial drop from surface to mid-depth was accompanied by a more moderate radial gradient, while the deep layer remained uniformly low.

3.5.2. Fluid velocity distributions in ECM, PCM, and chondrocytes

Fluid velocity fields in ECM, PCM, and chondrocytes varied spatially with depth, and radial position (Fig. 8b). The ECM exhibited the highest fluid velocity, exceeding 0.80 mm/s near the bottom-lateral boundaries. Within SZ, ECM fluid velocities varied from approximately 0.03 mm/s along the central axis to over 0.57 mm/s at the periphery. The PCM exhibited a similar spatially varying velocity distribution but 30–60%

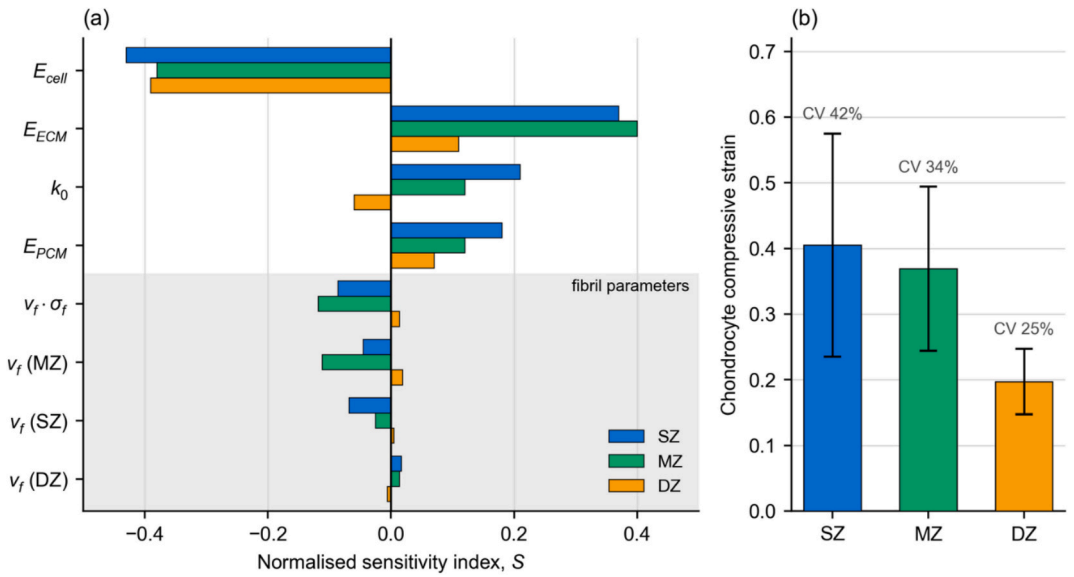

Fig. 9. Sensitivity and uncertainty of the predicted chondrocyte compressive strain. (a) Normalized sensitivity index, S, of the zone-averaged chondrocyte compressive strain to a ± 20% change in each model parameter, evaluated separately for the SZ, MZ, and DZ. A larger magnitude of S means the strain is more sensitive to that parameter; a positive S means increasing the parameter raises the strain, and a negative S means it lowers the strain. (b) Predicted zone-averaged chondrocyte compressive strain in each zone; the error bars are ±1 standard deviation (SD), obtained by propagating the parameter uncertainties through these sensitivity indices. The percentage above each bar is the coefficient of variation (CV = SD/mean × 100%), i.e., the uncertainty of the prediction relative to its mean value.

reduction compared to the ECM. In MZ, ECM fluid velocities reached 0.32–0.37 mm/s, while PCM velocities varied between 0.05 and 0.25 mm/s. Notably, chondrocytes occasionally exhibited fluid velocities comparable to or exceeding those in the surrounding PCM, particularly in regions of high cellular permeability. DZ demonstrated a distinct pattern where central ECM velocities fell below 0.02 mm/s, while lateral boundaries maintained peak velocities above 0.80 mm/s and localized areas within the chondrocyte region revealed similar increases in flow.

3.6. *Sensitivity and uncertainty analyses*

The sensitivity analyses (Fig. 9a) showed that the chondrocyte modulus was the most influential parameter in each zone (S = −0.43, −0.38 and − 0.39 in SZ, MZ and DZ), followed by the non-fibrillar ECM modulus (S = +0.37, +0.40 and + 0.11). The initial permeability (S = +0.21, +0.12 and − 0.06) and the pericellular modulus (S = +0.18, +0.12 and + 0.07) were of intermediate influence, whereas all four fibril parameters were comparatively weak (|S| ≤ 0.12) (Fig. 9a).

The uncertainty analysis by FOSM method gives a predicted zone-averaged chondrocyte compressive strain of 0.405 ± 0.170 in the SZ, 0.369 ± 0.125 in the MZ and 0.197 ± 0.050 in the DZ, corresponding to coefficients of variation of 42%, 34% and 25%, respectively (Fig. 9b).

4. Discussion

This study utilized a detailed microstructural based explicit multi-scale computational model to dissect the mechanical role of articular cartilage and its key constituents—type II collagen fibrillar network and non-fibrillar ground substances to estimate how macro-strains translate into micro-strains on chondrocytes under physiological loading conditions during daily activities (Deneweth et al., 2013; Elahi et al., 2021). The central contribution of the developed MS-FRPHE model is its ability to effectively capture stress trajectories in type II collagen fibrillar network and *in situ* chondrocyte mechanobiology. Because each fibril is represented as a separate connector element, the stress in any individual fibril is directly available at any location and is presented here as the stress pattern of the fibrillar network (Fig. 6). Homogenized formulations, used in earlier cell-scale models, cannot provide this output (Halloran et al., 2018; Tanska et al., 2020). Furthermore, the integration of chondrocyte and its cellular microenvironment with zone-specific geometry and density variations reflects the native distribution across cartilage layers (Ren et al., 2016), a unique aspect of the proposed model for coupling micro- and macroscale mechanics in a single construct. Simulating this high-fidelity cartilage model enhances our understanding of cartilage and *in situ* chondrocyte mechanobiology under physiological loading in greater detail.

The robustness of the MS-FRPHE model was established through the validation across multiple loading conditions and strain rates. At slow strain rate (0.1% s^{-1}), the model accurately predicted experimental peak forces for both indentation ($R^2 = 0.98$) and unconfined compression ($R^2 = 0.93$). At fast strain rate (100% s^{-1}), substantially higher peak forces were observed due to rapid fluid pressurization, with excellent model-experiment agreement ($R^2 = 0.97$–0.98). The ratio of peak forces between fast and slow strain rates was 12.0 for indentation and 6.8 for unconfined compression experimentally, reflecting the strain-rate dependent biphasic behavior characteristic of cartilage. The model captured this rate dependency well, predicting ratios of 11.6 and 7.2 for indentation and unconfined compression, respectively. Across all four conditions spanning a 1000-fold range in strain rates, the average R^2 was 0.97, demonstrating excellent agreement between experimental measurements and computational predictions and confirming the model's capability to capture the time-dependent interplay between solid matrix deformation and interstitial fluid flow.

The zone-wise strain contours across the ECM, PCM, and chondrocytes resembled distinct mechanical responses, reflecting the complex interplay between structural organization, matrix composition, and fluid pressurization. Our results revealed that the SZ, under high strain-rate loading, can momentarily experience lower strain than the MZ due to its dense, tangentially aligned collagen network and rapid poroelastic pressurization under constrained fluid flow (Li & Herzog, 2004). Low hydraulic permeability in SZ traps interstitial fluid during rapid loading, elevating pore pressure and stiffening the matrix, thereby limiting bulk deformation (Setton et al., 1993). This protective mechanism is consistent with the SZ primary function of resisting shear and tensile stresses at the articular surface (Karpiński et al., 2025). In contrast, the transitional architecture of the ECM in the MZ is associated with the highest

predicted matrix strain. Changes in collagen fibril orientation from tangential to random, combined with intermediate proteoglycan content, create a region of mechanical discontinuity that concentrates strain during compression. The isotropic fibril arrangement in MZ provides less structural resistance to compressive loading, allowing greater instantaneous compaction when fluid flow is constrained (Quiroga et al., 2017; Ravanfar & Yao, 2019). ECM experienced lower compressive strain with zone-wise variations compared with PCM (Fig. 4). PCM strains consistently exceed ECM values, indicating regions of strain amplification within the tissue. Such amplification may influence chondrocyte mechanotransduction although this remains to be established experimentally. This difference reflects the PCM's greater compliance and its capacity to accommodate deformation. PCM's composition and stiffness markedly influence cell-level strains, as observed in atomic force microscopy and micropipette aspiration experiments (McLeod et al., 2013; Wilusz et al., 2014). From a mechanobiological perspective, the SZ chondrocytes are more sensitive to shape changes and thus potentially at higher risk for injury when subjected to rapid or instantaneous loading (Argote et al., 2019; Bartell et al., 2015). These zone-specific deformation patterns suggest differential mechanotransduction responses. Furthermore, a relatively uniform chondrocyte deformation in deeper zones corresponds with experimentally observed columnar cell shapes, suggesting that these cells respond to more modest mechanical cues essential for steady-state cartilage homeostasis (Boos et al., 2022; Stok et al., 2025; van der Kraan et al., 2010).

The fibrillar network stress distributions conform with their orientation such that fibrils parallel to the surface in the SZ experience the maximum stress, whereas the fibrils oriented vertically in DZ withstand little to no stress. Our discrete connector element approach enabled explicit representation of individual collagen fibrils, allowing direct computation of fibrillar mechanics under physiological loading, a methodological advancement over previous homogenized fibril distribution models (Moore et al., 2023; Tan et al., 2023). This methodological advancement allowed us to capture the compression-tension nonlinearity inherent to cartilage mechanics, where SZ fibrils resist tensile stresses generated during compression while DZ fibrils remain mechanically disengaged due to their perpendicular orientation to the loading direction. The density and orientation-wise mechanical behavior of collagen fibrils are crucial (Meng et al., 2017; Shirazi & Shirazi-Adl, 2008) for clearly understanding the details of the cartilage micro- and macro-mechanical coupling. The collagen network modulates both the solid-phase stiffness and the fluid dynamics within cartilage, ensuring efficient load distribution and maintaining tissue integrity (Korhonen et al., 2006).

The MS-FRPHE model also demonstrated depth-dependent variations in pore pressure and fluid velocity under rapid unconfined compression. The SZ developed peak pore pressure due to low permeability and restricted fluid flow, thereby enhancing hydrostatic support and increasing effective stiffness (Elder & Athanasiou, 2009; Pattappa et al., 2019; Soltz & Ateshian, 2000). This localized pressure buildup plays a crucial role in the tissue's load-bearing capacity. MZ displayed intermediate pore pressure distribution, reflecting its heterogeneous fibril orientation that transiently impedes fluid flow. DZ exhibited lower pore pressure as the vertical collagen fibrils facilitate efficient fluid flow toward the subchondral bone. This systematic decrease in pore pressure from SZ to DZ illustrates cartilage's inherent mechanism for load absorption and transmission while protecting deeper structural components including chondrocytes from excessive compressive forces. Furthermore, the highest fluid velocities near the lateral boundaries of ECM and a steep radial gradient at the periphery in SZ reflected rapid interstitial fluid exchange due to high local pressurization in SZ, indicating the dynamic fluid exchange under high interstitial fluid pressure. In contrast, the consistent lower fluid velocities in PCM indicates that its lower permeability moderates fluid flow and acts as a hydrodynamic buffer at the cell interface. From the mechanistic viewpoint, these velocity gradients can induce shear stress on chondrocyte membranes by generating viscous drag proportional to the fluid's viscosity (Sharifi & Gharravi, 2019; Spiteri et al., 2008; Zhu et al., 2010). Such shear stress influences cellular mechanotransduction, affecting nutrient transport and signal transduction pathways essential for cartilage maintenance (Yeh et al., 2013; Zhu et al., 2010).

The sensitivity of cartilage mechanics to collagen fibril orientation is well-documented in prior studies that demonstrated how depth-dependent fibril architecture critically influences stress-strain distributions (Shirazi et al., 2008) (Mononen et al., 2012). Our model predictions align with these established findings, where tangentially oriented superficial fibrils bear maximum stress while vertically oriented DZ fibrils remain mechanically disengaged. In our parametric sensitivity analyses, the signs of the indices were also consistent with the prior parametric analysis of Tanska et al. (Tanska et al., 2020) in which a lower cellular non-fibrillar modulus produced greater cell deformation, a lower pericellular non-fibrillar modulus produced smaller cell deformation, and a lower ECM fibril network modulus produced greater cell deformation. It is apparent from the analyses that stiffening the ECM through its non-fibrillar matrix increased chondrocyte strain, whereas stiffening it through the fibril network reduced it. These two constituents act in opposite directions because the fibrils carry tension and restrain deformation, while the non-fibrillar modulus governs the stiffness contrast with the much softer chondrocyte. Critically, the zonal ordering of chondrocyte strain (SZ $>$ MZ $>$ DZ) was preserved under every perturbation, indicating that the principal conclusions are robust to parameter uncertainty within this range. The relative uncertainty followed the sensitivity indices, being largest in the SZ and smallest in the DZ.

One of the limitations of the current model lies within the axisymmetric modeling approach. We acknowledge that the axisymmetric cartilage model produces non-ellipsoidal chondron shapes upon 3D extrusion. While a full 3D model would represent the actual cellular architecture (Fig. 10), huge computational burden prevented us from modeling even minimal sample sizes (2.8 mm diameter $\times$ 1.2 mm height) due to geometry merging complexities with thousands of cells. To justify the current approach, we assumed that (1) high circumferential chondron density creates near-continuity that approximates the axisymmetric extrusion, and (2) similar stiffness between the cells and surrounding matrix reduces circumferential discontinuities. These assumptions were validated by comparing a small-scale 3D model with its axisymmetric counterpart, each containing six chondrons distributed within an ECM structure (Fig. 10). For the 3D model, chondrons were circumferentially distributed within a cylinder built by revolving the rectangular structure of the axisymmetric model, and both models were assigned identical fibril configurations, material properties, and loading protocols as the full-scale model. The relative differences in total cell circumferential forces and maximum Mises stresses between the two approaches were computed as a function of the inter-cellular spacing in the circumferential direction (Fig. 11). Results showed only 5–8% differences in cell forces and stresses for low-to-medium cell periodicity, supporting the validity of the proposed modeling approach in this study.

Second, although the zone-wise fibrillar and cellular distributions result in a high-resolution cartilage model, the bio-fidelity of the model is partially limited by focusing only on type II collagen fibril, ignoring minor collagens such as type VI that reinforces PCM and type IX that stabilize the collagen–proteoglycan network (Lanzer & Komenda, 1990; Zelenski et al., 2015) in territorial matrix. By neglecting these collagens, the MS-FRPHE model may underestimate the local microscale reinforcement and the overall mechanical integrity of the cellular microenvironment. Furthermore, the developed model incorporated only zone-specific differences in collagen content and cell geometry, heterogeneity in proteoglycan concentration, permeability, and crosslink density remains the same throughout the model (Krakowski et al., 2024; Szarko & Xia, 2012). Next, instead of human cartilage sample, bovine cartilage was used for model calibration and validation; however,

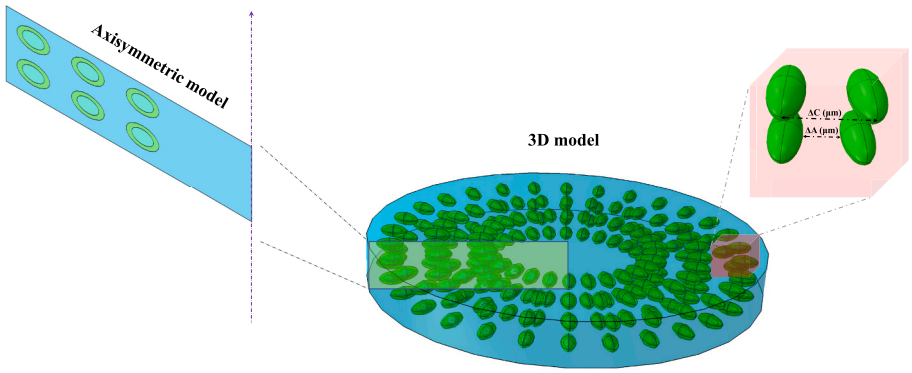

Fig. 10. Axisymmetric and 3D models are employed to test the validity of the current approach. ΔC (μm) and ΔA (μm) are the distance separating the centers of two successive cells in the circumferential direction and the proximity distance, respectively.

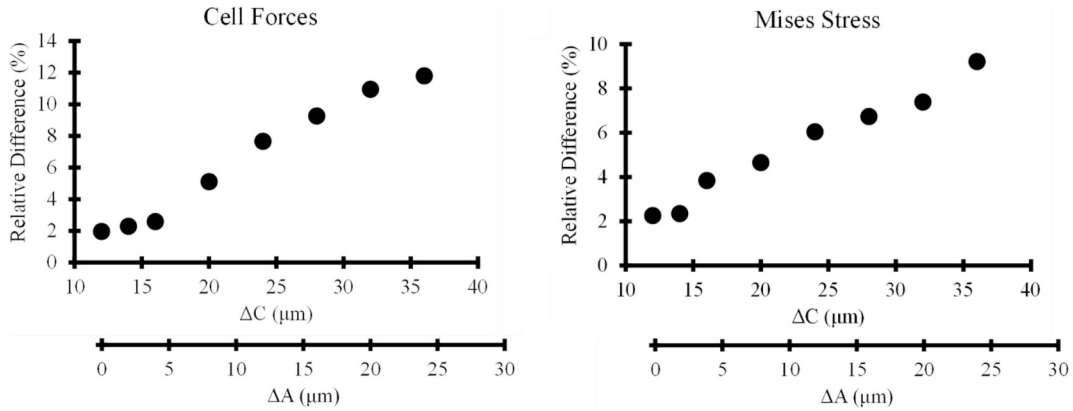

Fig. 11. The relative differences between 3D and axisymmetric model predictions (cell forces and maximum Mises stresses) as a function of the circumferential intercellular distance ΔC (μm) and the proximity distance ΔA (μm).

bovine cartilages showed well-documented structural and compositional similarity to human articular cartilage and were widely used for baseline comparison (Demarteau et al., 2006; Temple et al., 2016). Although species-specific differences in cell density, matrix composition, and mechanical properties may limit direct translation to human cartilage mechanics, we expect that species-specific calibration, and validation would provide comparable model performance. Finally, the adopted one-at-a-time sensitivity analysis is a local method evaluating isolated parameter changes around a baseline and unable to measure synergistic or combined effects between multiple input parameters, whereas variance-based global analysis apportions output variance across the entire input space including joint interactions. However, a variance-based global sensitivity analysis, which would require 50–100+ simulations for surrogate model training, remains beyond the present scope and is identified as a future work. Despite these limitations, the model demonstrated excellent agreement with experimental data (average $R^2 = 0.97$). Future studies will integrate minor collagen types and human tissue validation to substantiate the model's biofidelity.

In conclusion, this multiscale MS-FRPHE model provided insights into the depth-dependent mechanics of articular cartilage and *in situ* chondrocyte mechanobiology under physiological loading conditions. The integration of explicit fibrillar mechanics with cellular microenvironments provides constituent-level predictions that complement established tissue- and cell-scale models, revealing the zone-specific mechanics of the key constituents of cartilage. The model investigated the zone-specific mechanics of the fibrillar network, ECM, PCM, and chondrocytes whose size was reduced differentially across SZ (56%), MZ (49%), and DZ (21%). These predictions align with experimental data, providing a quantitative basis for the future study of cartilage micromechanics. By capturing the complex interplay between solid matrix deformation, fluid pressurization, and fibrillar reinforcement, this computational framework reproduces the bulk mechanical response across a 1000-fold range of strain rate and generates constituent-level predictions of the native tissue's zone-specific mechanical properties that require future experimental validation. Future refinements incorporating minor collagens and dynamic loading conditions will further enhance the model's predictive capabilities.

CRediT authorship contribution statement

Saiful Islam: Writing – review & editing, Writing – original draft, Visualization, Validation, Methodology, Investigation, Formal analysis, Data curation, Conceptualization. **Malek Adouni:** Writing – review & editing, Supervision, Conceptualization. **Asif Istiak:** Writing – original draft, Investigation. **Tanvir R. Faisal:** Writing – review & editing, Supervision, Project administration, Methodology, Conceptualization.

Declaration of competing interest

The authors declare that they have no known competing financial interests or personal relationships that could have appeared to influence the work reported in this paper.

Data availability

Data will be made available on request.

References

Adouni, M., Shirazi-Adl, A., Shirazi, R., 2012. Computational biodynamics of human knee joint in gait: from muscle forces to cartilage stresses. Journal of Biomechanics 45, 2149–2156.

Argote, P.F., Kaplan, J.T., Poon, A., Xu, X., Cai, L., Emery, N.C., Pierce, D.M., Neu, C.P., 2019. Chondrocyte viability is lost during high-rate impact loading by transfer of amplified strain, but not stress, to pericellular and cellular regions. Osteoarthritis and Cartilage 27, 1822–1830.

Ateshian, G.A., 2009. The role of interstitial fluid pressurization in articular cartilage lubrication. Journal of Biomechanics 42, 1163–1176.

Athanasiou, K., Darling, E.M., Hu, J.C., 2009. Articular cartilage tissue engineering. Morgan & Claypool Publishers.

Bartell, L.R., Fortier, L.A., Bonassar, L.J., Cohen, I., 2015. Measuring microscale strain fields in articular cartilage during rapid impact reveals thresholds for chondrocyte death and a protective role for the superficial layer. Journal of Biomechanics 48, 3440–3446.

Boos, M.A., Lamandé, S.R., Stok, K.S., 2022. Multiscale Strain Transfer in Cartilage. Front Cell Dev Biol 10, 795522.

Chahine, N.O., Wang, C.C., Hung, C.T., Ateshian, G.A., 2004. Anisotropic strain-dependent material properties of bovine articular cartilage in the transitional range from tension to compression. Journal of Biomechanics 37, 1251–1261.

Darling, E.M., Wilusz, R.E., Bolognesi, M.P., Zauscher, S., Guilak, F., 2010. Spatial mapping of the biomechanical properties of the pericellular matrix of articular cartilage measured in situ via atomic force microscopy. Biophys J 98, 2848–2856.

Demarteau, O., Pillet, L., Inaebnit, A., Borens, O., Quinn, T., 2006. Biomechanical characterization and in vitro mechanical injury of elderly human femoral head cartilage: comparison to adult bovine humeral head cartilage. Osteoarthritis and Cartilage 14, 589–596.

Deneweth, J.M., Newman, K.E., Sylvia, S.M., McLean, S.G., Arruda, E.M., 2013. Heterogeneity of tibial plateau cartilage in response to a physiological compressive strain rate. Journal of Orthopaedic Research 31, 370–375.

Elahi, S.A., Tanska, P., Mukherjee, S., Korhonen, R.K., Geris, L., Jonkers, I., Famaey, N., 2021. Guide to mechanical characterization of articular cartilage and hydrogel constructs based on a systematic in silico parameter sensitivity analysis. Journal of the Mechanical Behavior of Biomedical Materials 124, 104795.

Elder, B.D., Athanasiou, K.A., 2009. Hydrostatic pressure in articular cartilage tissue engineering: from chondrocytes to tissue regeneration. Tissue Eng Part B Rev. 15, 43–53.

Faisal, T.R., Adouni, M., Dhaher, Y.Y., 2019. The effect of fibrillar degradation on the mechanics of articular cartilage: a computational model. Biomechanics and Modeling in Mechanobiology 18, 733–751.

Faisal, T.R., Adouni, M., Dhaher, Y.Y., 2023. Surrogate modeling of articular cartilage degradation to understand the synergistic role of MMP-1 and MMP-9: a case study. Biomechanics and Modeling in Mechanobiology 22, 43–56.

Federico, S., Grillo, A., La Rosa, G., Giaquinta, G., Herzog, W., 2005. A transversely isotropic, transversely homogeneous microstructural-statistical model of articular cartilage. Journal of Biomechanics 38, 2008–2018.

Flory, P.J., 1961. Thermodynamic relations for high elastic materials. Transactions of The Faraday Society 57, 829–838.

Fortin, M., Soulhat, J., Shirazi-Adl, A., Hunziker, E., Buschmann, M.D., 2000. Unconfined compression of articular cartilage: nonlinear behavior and comparison with a fibril-reinforced biphasic model. J. Biomech. Eng. 122, 189–195.

Grillo, A., Carfagna, M., Federico, S., 2017. Non-Darcian flow in fiber-reinforced biological tissues. Meccanica 52, 3299–3320.

Halloran, J.P., Sibole, S.C., Erdemir, A., 2018. The potential for intercellular mechanical interaction: simulations of single chondrocyte versus anatomically based distribution. Biomechanics and Modeling in Mechanobiology 17, 159–168.

Hamby, D., 1995. A comparison of sensitivity analysis techniques. Health Physics 68, 195–204.

Haut, R.C., Little, R.W., 1972. A constitutive equation for collagen fibers. Journal of Biomechanics 5, 423–430.

Holmes, M., Mow, V.C., 1990. The nonlinear characteristics of soft gels and hydrated connective tissues in ultrafiltration. Journal of Biomechanics 23, 1145–1156.

Hunziker, E.B., 1992, Articular cartilage staructure in humans and experimental animals. In: Kuettner, KE, Schleyerbach, R, Peyron, JG, Hascall, VC (Eds.), Articular Cartilage and osteoarthritis. pp. 1983-1999.

Hunziker, E.B., Quinn, T.M., Häuselmann, H.J., 2002. Quantitative structural organization of normal adult human articular cartilage. Osteoarthritis and Cartilage 10, 564–572.

Istiak, A., Islam, S., Adouni, M., Faisal, T.R., 2025a. Hyperelastic constitutive modeling of healthy and enzymatically mediated degraded articular cartilage. Biomechanics and Modeling in Mechanobiology 24, 471–487.

Istiak, A., Lawrence, A., Boesel, J., Kayes, M.I., Moni, A.S.B., Faisal, T.R., 2025b. Therapeutic potential of COMP and TIMP-3 in preserving cartilage integrity compromised by proteases: A histo-mechanical study. Journal of the Mechanical Behavior of Biomedical Materials 172, 107183.

Jadin, K.D., Wong, B.L., Bae, W.C., Li, K.W., Williamson, A.K., Schumacher, B.L., Price, J. H., Sah, R.L., 2005. Depth-varying density and organization of chondrocytes in immature and mature bovine articular cartilage assessed by 3d imaging and analysis. Journal of Histochemistry & Cytochemistry 53, 1109–1119.

Julkunen, P., Wilson, W., Jurvelin, J.S., Korhonen, R.K., 2009. Composition of the pericellular matrix modulates the deformation behavior of chondrocytes in articular cartilage under static loading. Med Biol Eng Comput 47, 1281–1290.

Julkunen, P., Jurvelin, J.S., Isaksson, H., 2010. Contribution of tissue composition and structure to mechanical response of articular cartilage under different loading geometries and strain rates. Biomechanics and Modeling in Mechanobiology 9, 237–245.

Julkunen, P., Wilson, W., Isaksson, H., Jurvelin, J.S., Herzog, W., Korhonen, R.K., 2013. A review of the combination of experimental measurements and fibril-reinforced modeling for investigation of articular cartilage and chondrocyte response to loading. Computational and Mathematical Methods in Medicine 2013, 326150.

Karpiński, R., Prus, A., Baj, J., Radej, S., Prządka, M., Krakowski, P., Jonak, K., 2025. Articular Cartilage: Structure, Biomechanics, and the Potential of Conventional and Advanced Diagnostics. Applied Sciences 15, 6896.

Khoshgoftar, M., Torzilli, P.A., Maher, S.A., 2018. Influence of the pericellular and extracellular matrix structural properties on chondrocyte mechanics. J Orthop Res 36, 721–729.

Kim, E., Guilak, F., Haider, M.A., 2008. The dynamic mechanical environment of the chondrocyte: a biphasic finite element model of cell-matrix interactions under cyclic compressive loading. Journal of Biomechanical Engineering 130 (6), 061009.

Korhonen, R.K., Laasanen, M.S., Töyräs, J., Lappalainen, R., Helminen, H.J., Jurvelin, J. S., 2003. Fibril reinforced poroelastic model predicts specifically mechanical behavior of normal, proteoglycan depleted and collagen degraded articular cartilage. Journal of Biomechanics 36, 1373–1379.

Korhonen, R.K., Julkunen, P., Rieppo, J., Lappalainen, R., Konttinen, Y.T., Jurvelin, J.S., 2006. Collagen network of articular cartilage modulates fluid flow and mechanical stresses in chondrocyte. Biomechanics and Modeling in Mechanobiology 5, 150–159.

Krakowski, P., Rejniak, A., Sobczyk, J., Karpiński, R., 2024. Cartilage Integrity: A Review of Mechanical and Frictional Properties and Repair Approaches in Osteoarthritis. Healthcare (Basel) 12.

Lanzer, W.L., Komenda, G., 1990. Changes in articular cartilage after meniscectomy. Clin Orthop Relat Res 41–48.

Li, L.P., Herzog, W., 2004. Strain-rate dependence of cartilage stiffness in unconfined compression: the role of fibril reinforcement versus tissue volume change in fluid pressurization. Journal of Biomechanics 37, 375–382.

Li, L., Soulhat, J., Buschmann, M.D., Shirazi-Adl, A., 1999. Nonlinear analysis of cartilage in unconfined ramp compression using a fibril reinforced poroelastic model. Clinical Biomechanics 14, 673–682.

Li, L., Cheung, J.T.-M., Herzog, W., 2009. Three-dimensional fibril-reinforced finite element model of articular cartilage. Medical & Biological Engineering & Computing 47, 607–615.

McLeod, M.A., Wilusz, R.E., Guilak, F., 2013. Depth-dependent anisotropy of the micromechanical properties of the extracellular and pericellular matrices of articular cartilage evaluated via atomic force microscopy. Journal of Biomechanics 46, 586–592.

Meng, Q., An, S., Damion, R.A., Jin, Z., Wilcox, R., Fisher, J., Jones, A., 2017. The effect of collagen fibril orientation on the biphasic mechanics of articular cartilage. Journal of the Mechanical Behavior of Biomedical Materials 65, 439–453.

Mononen, M.E., Mikkola, M.T., Julkunen, P., Ojala, R., Nieminen, M.T., Jurvelin, J.S., Korhonen, R.K., 2012. Effect of superficial collagen patterns and fibrillation of femoral articular cartilage on knee joint mechanics-a 3D finite element analysis. Journal of Biomechanics 45, 579–587.

Moore, A.C., Hennessy, M.G., Nogueira, L.P., Franks, S.J., Taffetani, M., Seong, H., Kang, Y.K., Tan, W.S., Miklosic, G., El Laham, R., Zhou, K., Zharova, L., King, J.R., Wagner, B., Haugen, H.J., Münch, A., Stevens, M.M., 2023. Fiber reinforced hydrated networks recapitulate the poroelastic mechanics of articular cartilage. Acta Biomaterialia 167, 69–82.

Morgan, F., 1960. Mechanical properties of collagen and leather fibers. Am Leather Chem Assoc J 55, 23–24.

Mow, V.C., 1991. Structure and function of articular cartilage and meniscus. Basic orthopaedic biomechanics 143–198.

Nahian, A., Sapra, A., 2020. Histology. Chondrocytes.

Oungoulian, S.R., Chen, S.S., Davol, A., Sah, R.L., Klisch, S.M., 2007. Year Extended two compartmental swelling stress model and isotropic cauchy stress equation for articular cartilage proteoglycans. In: Summer Bioengineering Conference.

Park, S., Hung, C., Ateshian, G., 2004. Mechanical response of bovine articular cartilage under dynamic unconfined compression loading at physiological stress levels. Osteoarthritis and Cartilage 12, 65–73.

Pattappa, G., Zellner, J., Johnstone, B., Docheva, D., Angele, P., 2019. Cells under pressure - the relationship between hydrostatic pressure and mesenchymal stem cell chondrogenesis. Eur Cell Mater 37, 360–381.

Pierce, D.M., 2022. Multi-phase, large-strain constitutive models of cartilage for finite element analyses in 3-D. Archive of Applied Mechanics 92, 513–528.

Pierce, D.M., Trobin, W., Trattnig, S., Bischof, H., Holzapfel, G.A., 2009. A phenomenological approach toward patient-specific computational modeling of articular cartilage including collagen fiber tracking. J Biomech Eng 131 (9), 091006.

Quiroga, J.M.P., Wilson, W., Ito, K., van Donkelaar, C.C., 2017. Relative contribution of articular cartilage's constitutive components to load support depending on strain rate. Biomechanics and Modeling in Mechanobiology 16, 151–158.

Ravanfar, M., Yao, G., 2019. Simultaneous tractography and elastography imaging of the zone-specific structural and mechanical responses in articular cartilage under compressive loading. Biomed. Opt. Express 10, 3241–3256.

Ren, X., Wang, F., Chen, C., Gong, X., Yin, L., Yang, L., 2016. Engineering zonal cartilage through bioprinting collagen type II hydrogel constructs with biomimetic chondrocyte density gradient. BMC Musculoskeletal Disorders 17, 301.

Responte, D.J., Natoli, R.M., Athanasiou, K.A., 2007. Collagens of articular cartilage: structure, function, and importance in tissue engineering. Critical Reviews™. Biomedical Engineering 35.

Sajjadinia, S.S., Haghpanahi, M., Razi, M., 2019. Computational simulation of the multiphasic degeneration of the bone-cartilage unit during osteoarthritis via indentation and unconfined compression tests. Proceedings of the Institution of Mechanical Engineers, Part H: Journal of Engineering in Medicine 233, 871–882.
Schinagl, R.M., Gurskis, D., Chen, A.C., Sah, R.L., 1997. Depth-dependent confined compression modulus of full-thickness bovine articular cartilage. Journal of Orthopaedic Research 15, 499–506.
Seifzadeh, A., Wang, J., Oguamanam, D., Papini, M., 2011. A nonlinear biphasic fiber-reinforced porohyperviscoelastic model of articular cartilage incorporating fiber reorientation and dispersion. Journal of Biomechanical Engineering 133 (8), 81004.
Setton, L.A., Zhu, W., Mow, V.C., 1993. The biphasic poroviscoelastic behavior of articular cartilage: role of the surface zone in governing the compressive behavior. Journal of Biomechanics 26, 581–592.
Sharifi, N., Gharravi, A.M., 2019. Shear bioreactors stimulating chondrocyte regeneration, a systematic review. Inflammation and Regeneration 39, 16.
Shioji, S., Imai, S., Ando, K., Kumagai, K., Matsusue, Y., 2014. Extracellular and intracellular mechanisms of mechanotransduction in three-dimensionally embedded rat chondrocytes. PLoS One 9, e114327.
Shirazi, R., Shirazi-Adl, A., 2005. Analysis of articular cartilage as a composite using nonlinear membrane elements for collagen fibrils. Medical Engineering & Physics 27, 827–835.
Shirazi, R., Shirazi-Adl, A., 2008. Deep vertical collagen fibrils play a significant role in mechanics of articular cartilage. J Orthop Res 26, 608–615.
Shirazi, R., Shirazi-Adl, A., Hurtig, M., 2008. Role of cartilage collagen fibrils networks in knee joint biomechanics under compression. Journal of Biomechanics 41, 3340–3348.
Simo, J.C., Lubliner, J., 1986. Formulation and Computational Aspects of a Three-Dimensional Finite Strain Viscoelastic Damage Model. SAE Transactions 95, 220–229.
Soltz, M.A., Ateshian, G.A., 2000. Interstitial fluid pressurization during confined compression cyclical loading of articular cartilage. Ann Biomed Eng 28, 150–159.
Spiteri, C.G., Young, E.W.K., Simmons, C.A., Kandel, R.A., Pilliar, R.M., 2008. Substrate architecture and fluid-induced shear stress during chondrocyte seeding: Role of α5β1 integrin. Biomaterials 29, 2477–2489.
Stok, K.S., Boos, M.A., Disney, C., Lerdbussakaram, T., Müller, R., 2025. Quantitative Microstructural Imaging and Mechanics of Cartilage Using Experimental and Computational Approaches, Bioimaging in Tissue Engineering and Regeneration: Advanced Microscopy and Preclinical Imaging. Springer, pp. 1–38.
Suh, J.-K., Spilker, R.L., 1994. Indentation analysis of biphasic articular cartilage: nonlinear phenomena under finite deformation. Journal of Biomechanical Engineering 116 (1), 1–9.
Szarko, M., Xia, Y., 2012. Direct Visualization of the Depth-Dependent Mechanical Properties of Full-Thickness Articular Cartilage. Open J Orthop 2.
Szarko, M., Muldrew, K., Bertram, J.E., 2010. Freeze-thaw treatment effects on the dynamic mechanical properties of articular cartilage. BMC Musculoskeletal Disorders 11, 231.
Tan, W.S., Moore, A.C., Stevens, M.M., 2023. Minimum design requirements for a poroelastic mimic of articular cartilage. J Mech Behav Biomed Mater 137, 105528.
Tanska, P., Venäläinen, M.S., Erdemir, A., Korhonen, R.K., 2020. A multiscale framework for evaluating three-dimensional cell mechanics in fibril-reinforced poroelastic tissues with anatomical cell distribution – Analysis of chondrocyte deformation behavior in mechanically loaded articular cartilage. Journal of Biomechanics 101, 109648.
Temple, D.K., Cederlund, A.A., Lawless, B.M., Aspden, R.M., Espino, D.M., 2016. Viscoelastic properties of human and bovine articular cartilage: a comparison of frequency-dependent trends. BMC Musculoskeletal Disorders 17, 419.
van der Kraan, P.M., Blaney Davidson, E.N., van den Berg, W.B., 2010. A role for age-related changes in TGFbeta signaling in aberrant chondrocyte differentiation and osteoarthritis. Arthritis Res Ther 12, 201.
Van der Voet, A., 1997. A comparison of finite element codes for the solution of biphasic poroelastic problems. Proceedings of the Institution of Mechanical Engineers. Part H, Journal of Engineering in Medicine 211, 209–211.
Wang, C.C., Hung, C.T., Mow, V.C., 2001. An analysis of the effects of depth-dependent aggregate modulus on articular cartilage stress-relaxation behavior in compression. Journal of Biomechanics 34, 75–84.
Wilson, W., Van Donkelaar, C., Van Rietbergen, B., Ito, K., Huiskes, R., 2004. Stresses in the local collagen network of articular cartilage: a poroviscoelastic fibril-reinforced finite element study. Journal of biomechanics 37, 357–366.
Wilson, W., Van Donkelaar, C., Van Rietbergen, B., Huiskes, R., 2005. A fibril-reinforced poroviscoelastic swelling model for articular cartilage. Journal of biomechanics 38, 1195–1204.
Wilson, W., Huyghe, J., Van Donkelaar, C., 2006. A composition-based cartilage model for the assessment of compositional changes during cartilage damage and adaptation. Osteoarthritis and Cartilage 14, 554–560.
Wilusz, R.E., Sanchez-Adams, J., Guilak, F., 2014. The structure and function of the pericellular matrix of articular cartilage. Matrix Biology 39, 25–32.
Yeh, C.-C., Chang, S.-F., Huang, T.-Y., Chang, H.-I., Kuo, H.-C., Wu, Y.-C., Hsieh, C.-H., Shi, C.-S., Chen, C.-N., 2013. Shear stress modulates macrophage-induced urokinase plasminogen activator expression in human chondrocytes. Arthritis research & therapy 15, 1–13.
Youn, I., Choi, J., Cao, L., Setton, L., Guilak, F., 2006. Zonal variations in the three-dimensional morphology of the chondron measured in situ using confocal microscopy. Osteoarthritis and cartilage 14, 889–897.
Zelenski, N.A., Leddy, H.A., Sanchez-Adams, J., Zhang, J., Bonaldo, P., Liedtke, W., Guilak, F., 2015. Type VI Collagen Regulates Pericellular Matrix Properties, Chondrocyte Swelling, and Mechanotransduction in Mouse Articular Cartilage. Arthritis Rheumatol 67, 1286–1294.
Zhao, Z., Li, Y., Wang, M., Zhao, S., Zhao, Z., Fang, J., 2020. Mechanotransduction pathways in the regulation of cartilage chondrocyte homoeostasis. Journal of cellular and molecular medicine 24, 5408–5419.
Zhu, F., Wang, P., Lee, N.H., Goldring, M.B., Konstantopoulos, K., 2010. Prolonged application of high fluid shear to chondrocytes recapitulates gene expression profiles associated with osteoarthritis. PloS one 5, e15174.